Letter Vol. 6, No. 10 / October 2019 / Optica 1338

optica

Efficient terahertz and Brunel harmonic generation from air plasma via mid-infrared coherent control

DOGEUN JANG, ROBERT M. SCHWARTZ, DANIEL WOODBURY, JESSE GRIFF-MCMAHON, ABDURRAHMAN H. YOUNIS, HOWARD M. MILCHBERG, AND KI-YONG KIM*

Institute for Research in Electronics and Applied Physics, University of Maryland, College Park, Maryland 20742, USA
*Corresponding author: kykim@umd.edu

Received 28 May 2019; revised 3 September 2019; accepted 15 September 2019 (Doc. ID 368389); published 10 October 2019

Nonlinear light conversion involves one or more bound–bound, bound–free, free–free, and free–bound transitions. It is often challenging to interpret the exact conversion mechanisms. Here we use a femtosecond mid-infrared laser to enhance free–free transitions in terahertz and Brunel harmonic generation from air plasma. Microscopically, both THz and harmonics originate from a common source–ionization-induced plasma currents–and are greatly enhanced when driven by intense long-wavelength pulses. We observe 1% laser-to-terahertz conversion efficiency. Using two-color laser fields, we generate coherent radiation from terahertz to petahertz and investigate the interplay among tunneling ionization, terahertz, and harmonic generation with coherent control.

https://doi.org/10.1364/OPTICA.6.001338

Two-color laser mixing in gas has been widely used as an intense broadband terahertz (THz) source in many applications [1–18]. In this scheme, a femtosecond laser pulse (ω) and its second harmonic (2ω) are co-focused to ionize a gas and create a plasma current. Under the right phase difference between the two-color laser fields, a directional current can arise on the time scale of the laser pulse duration, which emits THz radiation in the far field [5–7].

Ionization-induced plasma currents can also produce harmonic radiation as originally proposed by Brunel [19]. This Brunel harmonic radiation (free–free) is emitted from an ensemble of free electrons oscillating nonsinusoidally in time as a result of phase-dependent tunneling ionization [19]. This is also responsible for low-order harmonics typically up to the 9th order [20], whereas high-order harmonics are largely produced by electron–ion recollision (free–bound) [21]. THz radiation arising from free–free transitions can be considered as the 0th order Brunel radiation since both arise from the same plasma current.

Low-order harmonics can also be produced by nonlinear bound electron polarization. At a single atom level, this bound–bound contribution, however, can be dominated by the plasma current when driven by intense long-wavelength pulses. This happens because the electron quiver velocity (or plasma current) increases with a wavelength ($v_e \propto \lambda$) at a constant laser intensity, whereas the third-order nonlinear susceptibility $\chi^{(3)}$ from bound electrons, the dominant lowest-order for centrosymmetric media, exhibits no wavelength-favorable dependence [22]. This trend is confirmed in a recent time-dependent Schrödinger equation (TDSE) simulation [23] (see Supplement 1 for a semiclassical calculation). Furthermore, the contribution from free-bound recollision dramatically decreases as the driver laser wavelength increases [23,24]. This was observed in theoretical [25] and experimental [26] studies, both reporting a high-order harmonic yield scaling of $\lambda^{-(5\sim6.5)}$. Thus, a long-wavelength setting provides an ideal testbed to study plasma currents as a main source for both THz and low-order harmonic generation with reduced involvement from other nonlinear mechanisms. With increasing laser wavelength, the nature of ionization also shifts from multiphoton to tunneling regimes, where laser phase-dependent electron dynamics plays a key role in new frequency generation. Previously, simultaneous measurements of THz and harmonics were conducted at near-infrared (0.8 μm) laser wavelengths [15,27,28], and those studies were limited to high-order harmonics (>16th), neither observing nor considering lower-order harmonics.

In two-color laser fields, the plasma current obtains a drift velocity that scales linearly with wavelength ($v_d \propto \lambda$) [5], like the electron quiver velocity. Thus, for fixed laser intensity, both THz and Brunel harmonic energies are expected to scale with λ^2. A recent experiment conducted at $\lambda = 0.8 - 2$ μm, however, shows a surprisingly high THz energy scaling as $\propto \lambda^{4.6}$ [11]. Although this dependence may be explained by high-order plasma currents [11], additional experiments at longer laser wavelengths are desirable to better understand wavelength-dependent THz generation [16–18].

Our experiment was performed with an optical parametric chirped pulse amplification (OPCPA) laser capable of delivering 3.9 μm, 30 mJ, 80 fs pulses at a repetition rate of 20 Hz [29–31]. A schematic of our experimental layout is shown in Fig. 1. To generate two-color laser fields, a thin GaSe crystal is used for second harmonic generation (SHG) [32,33]. The crystal shows the azimuthal angle (α) dependent second harmonic (SH) and THz generation, as shown in Fig. 2. Due to fact that the GaSe crystal has D_{3h} threefold symmetry [34], both SH and THz signals exhibit a 60° rotational period. We observe both Type 0 and

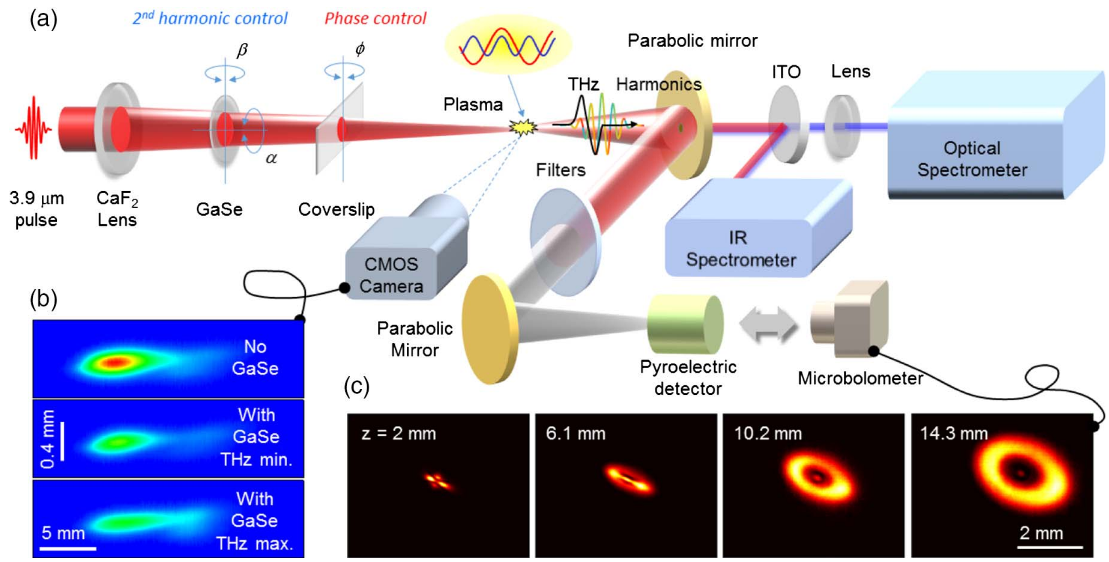

Fig. 1. Schematic of two-color, mid-infrared laser mixing in air for THz and harmonic generation and characterization. (a) Experimental setup. Mid-infrared pulses (3.9 μm, 120 fs, 1–5 mJ) are focused by a CaF_2 lens with focal length of 200 mm in air at 1 atm. (See Supplement 1.) (b) Plasma fluorescence side-imaged by a monochrome CMOS camera (Thorlabs, Quantalux) without and with the GaSe crystal at the glass tilt angle of $\phi = 28°$ and 42°. (c) Conical THz radiation profiles at various distances from the end of the air plasma imaged by the microbolometer.

Type 1 SHG with the GaSe crystal (see Supplement 1). Here, THz generation is dominantly governed by Type 0 SHG, in which both the ω and 2ω pulses are linearly polarized along the extraordinary axis of GaSe ($\alpha = 30°, 90°, 150°$). This configuration yields much greater THz radiation compared to the case where the two-color fields are perpendicularly polarized ($\alpha = 0°, 60°, 120°, 180°$). The resulting THz radiation is also linearly polarized along the laser field direction.

In two-color laser fields, $E_L(t) = E_\omega(t)\cos(\omega t) + E_{2\omega}(t)\cos(2\omega t + \theta)$, where θ is the relative phase between the fundamental (E_ω) and second harmonic ($E_{2\omega}$) fields, we can study phase-dependent tunneling ionization and subsequent plasma-current-induced Brunel radiation. In our scheme, the

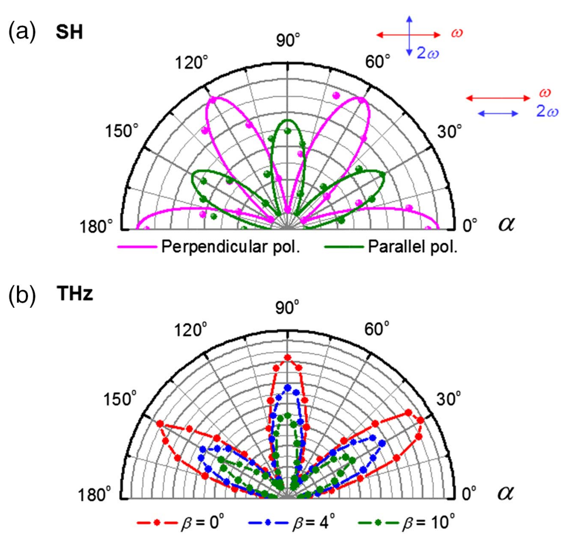

Fig. 2. Second harmonic (SH) and THz generation from GaSe. (a) SH (1.95 μm) yield as a function of the crystal rotation angle α at $\beta = 0$, with polarization parallel (green dots) or perpendicular (magenta dots) to the incoming horizontal polarization at 3.9 μm. (b) THz yield as a function of α at $\beta = 0°$, 4°, and 10°.

initial relative phase θ_0 is controlled by using material dispersion inside a thin coverslip glass placed after the GaSe crystal at angle ϕ from the laser axis (see Fig. 1 and Supplement 1). In the tunneling regime, the ionization rate is highly nonlinear and strongly enhanced when the two-color wave crests are in phase with $\theta = 0$, but this results in less THz radiation according to the plasma current model [5]. Note that the optimum phases for peak ionization rate and for THz generation differ by $\pm\pi/2$.

This phase-dependent ionization is evident from plasma fluorescence signatures remaining long after rapid tunneling ionization, as shown in Figs. 3(a) and 3(b). Note that the initial relative phase θ_0 in the plot is arbitrarily defined ($\theta_0 = 0$ when the coverslip is normal to the laser at $\phi = 0°$), whereas the relative phase θ at z can be determined from local plasma fluorescence intensities. For instance, the points marked with X in Fig. 3(b) yield the lowest local fluorescence yields, thus $\theta = \pm\pi/2$. Note that a full extraction of $\theta(r, z, \theta_0, t)$ is difficult because of spatial (r, z) and temporal (t) variations of the two-color laser pulses with propagation. Here we consider an effective $\theta(z, \theta_0)$ that contributes to the THz signal most as we tilt the coverslip. The fluorescence variation along z at $\theta_0 = 0.9\pi$, which yields maximal far-field THz radiation, is plotted in Fig. 3(c) with local THz emission intensities determined by an aperture scanning method [8]. As the relative phase θ varies along z due to plasma dispersion and Gouy phase shifts, at $\theta_0 = 0.4\pi$ where minimal THz radiation emits overall, most THz radiation arises from $z \approx 15$ mm with $\theta = \pm\pi/2$. This radiation is much weaker than that at $\theta_0 = 0.9\pi$ because it originates ~0.8 Rayleigh length away from the laser focus. The corresponding THz radiation profiles are shown in Figs. 3(d) and 3(e). They exhibit characteristic conical emission, consistent with previous observations in near-infrared two-color laser mixing [8,10,12]. Also, the difference in size confirms their phase-dependent origin of emission.

We note that the secondary fluorescence hump observed around $z \approx 15$ mm in Fig. 3(b) is caused by an uncontrolled aberration in our beam focusing, also observed in the single-color

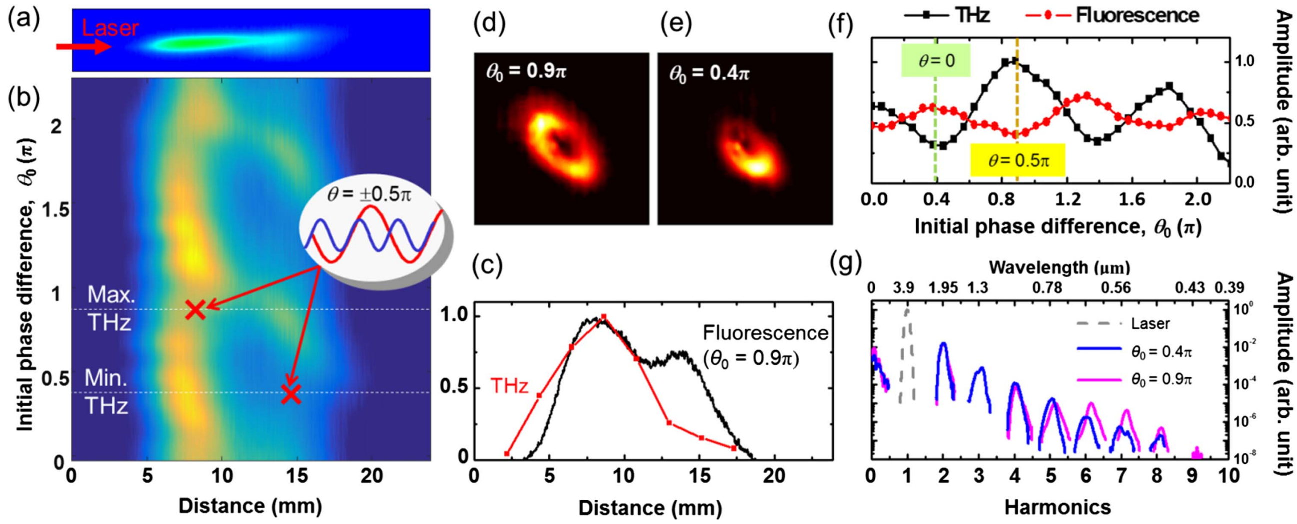

Fig. 3. Phase-dependent ionization and THz/harmonic generation. (a) Plasma fluorescence detected by side imaging when maximal THz radiation is emitted in the forward direction. The laser pulses are focused at $z \approx 8$ mm at peak intensities of 1.3×10^{14} W/cm^2 with a beam half width at half maximum (HWHM) of 60 μm. The Rayleigh length is estimated to be 8.5 mm under a Gaussian beam propagation assumption. (b) Radially integrated plasma fluorescence from (a) is plotted as a function of the initial relative phase θ_0 and the beam propagation distance z. Here $\theta_0 = 0$ is defined with the coverslip tilt angle at $\phi = 0°$. (c) Plasma fluorescence (black line) and THz local emission strength (red line) at $\theta_0 = 0.9\pi$ with THz radiation profiles captured at (d) $\theta_0 = 0.9\pi$ and (e) $\theta_0 = 0.4\pi$. (f) THz yield (black line), plasma fluorescence (red line) integrated from $z = 5$ mm to 10 mm. Here the relative phase $\theta = 0$ is determined when the local plasma fluorescence signal is maximal ($\theta = \pm\pi/2$ for minimal). (g) Measured THz and harmonic spectra obtained at $\theta_0 = 0.4\pi$ (blue line, minimal THz) and $\theta_0 = 0.9\pi$ (magenta line, maximal THz).

case in Fig. 1(b). Figures 3(f) and 3(g) show phase-dependent plasma fluorescence, THz, and low-order harmonics (up to the 9th order) yields. All exhibit strong phase-dependent modulations. The THz and fluorescence (or ionization rate) signals are clearly anti-correlated as shown in Fig. 3(f), consistent with the plasma current model [5]. Figure 3(g) shows measured radiation from 0th to 9th order, which exhibits coherent radiation from terahertz to petahertz frequencies under phase control ($\theta_0 = 0.4\pi$ versus 0.9π). The emitted THz spectrum is characterized by a Michelson-type Fourier transform infrared (FTIR) spectrometer.

Figure 4(a) shows measured field autocorrelations (inset) and corresponding spectra obtained via Fourier transformation. The radiation peaks at 12 THz with a bandwidth exceeding 30 THz. Also, the THz output rapidly increases with laser energy as shown in Fig. 4(b). The maximum laser-to-THz conversion efficiency reaches ~1% even with a relatively low SH energy ratio of $|E_{2\omega}/E_\omega|^2 = 0.02$ (see Supplement 1). Along with other previous measurements [11,12], our experiment shows a wavelength-dependent scaling of $\lambda^{2.6}$ for THz conversion efficiency as shown in Fig. 4(c). We note that this scaling is not absolute and largely depends on the energy ratio $|E_{2\omega}/E_\omega|^2$. Due to our low energy ratio 0.02 compared to ~0.1 at 800 nm [12] and 0.05 at 1.2 ~ 1.8 μm [11], our result provides a lower limit of scaling. Nonetheless, our scaling agrees well with some variants, $\lambda^{2.55\sim2.75}$, obtained from 0.8–2 μm [16,18]. Figure 5(a) displays all measured phase-dependent harmonic (2nd–9th) yields. Those agree well with our simulation [Fig. 5(b)] based on a unidirectional pulse propagation equation model (see Supplement 1) [35,36]. Through the simulation, we confirm that the plasma current-induced Brunel mechanism is dominant over bound electron effects for THz generation [see Fig. 5(c)]. The simulation predicts ~1% efficiency, consistent with the measurement. However, for harmonic (3rd ~ 5th), the bound electron effect cannot be ignored because the combined ($\chi^{(3)}$ plus plasma) effects contribute much more than the plasma effect alone. It is possibly due to synergistic effects between those two such as $\chi^{(3)}$-based cascade

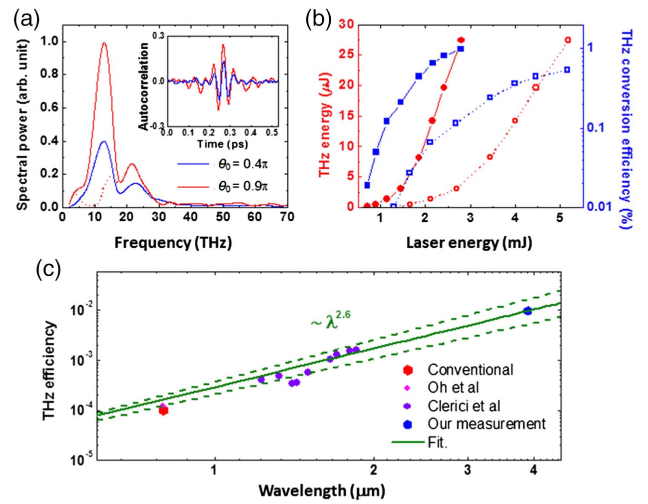

Fig. 4. THz spectrum and conversion efficiency. (a) Measured THz field autocorrelations (inset) and spectra obtained at two different initial relative phases $\theta_0 = 0.4\pi$ (blue line) and $\theta_0 = 0.9\pi$ (red line), which yield minimal and maximal THz radiation, respectively. Note that the THz waveforms and spectrum are distorted at <18 THz (dotted line) by the 7 μm longpass filters used to cutoff the laser and high-frequency (>40 THz) components. This artifact is corrected by considering the transmission curve of the filters (solid lines). (b) THz output energy (red lines) and corresponding laser-to-THz conversion efficiency (blue lines) as functions of the laser energy measured just before the CaF_2 lens (dotted lines) and estimated after the coverslip (solid lines). (c) THz generation efficiency as a function of the fundamental wavelength in two-color laser mixing.

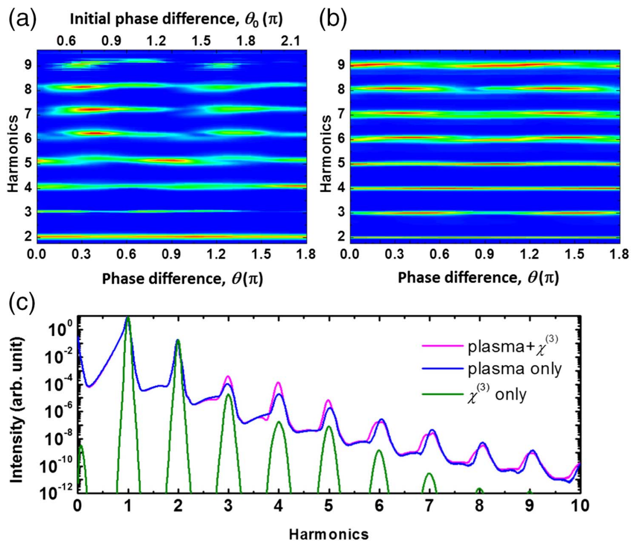

Fig. 5. Coherent control of harmonic electromagnetic waves. (a) Measured and (b) simulated phase-dependent harmonic (2nd–9th) yields plotted as a function of θ at $z = 8$ mm, with each harmonic normalized to its maximal spectral power. The 3rd and 9th harmonics in (a) are not properly normalized due to their poor signal-to-noise. (c) Phase-averaged THz and harmonic spectra obtained from (b) comparing plasma and $\chi^{(3)}$ contributions.

mixing of plasma-produced Brunel radiation, $\chi^{(3)}$-induced beam self-focusing, and enhanced phase-matching of $\chi^{(3)}$-induced harmonics due to plasma formation (see Supplement 1). All these make it difficult to separate those two contributions in a macroscopic beam propagation setting [37,38].

In conclusion, we report the generation of coherent radiation from THz to ultraviolet via two-color laser mixing at the mid-infrared level. Here we make simultaneous measurements of THz and low-order harmonic radiation under common phase control. In practice, we achieve significant laser-to-THz conversion efficiency (~1%), about $10 \sim 100$ times larger than conventional values obtained with 0.8 μm lasers. The efficiency can be enhanced further with more efficient SHG. This type of source can potentially produce single-cycle, broadband, millijoule-level THz radiation, which is useful for studying THz-driven extreme nonlinearities.

Funding. Office of Naval Research (N00014-17-1-2705); Air Force Office of Scientific Research (FA9550-16-1-0163); SSGF program (DE-NA0003864).

Acknowledgment. Daniel Woodbury acknowledges support from SSGF program.

See Supplement 1 for supporting content.

REFERENCES

1. D. J. Cook and R. M. Hochstrasser, Opt. Lett. **25**, 1210 (2000).
2. M. Kress, T. Löffler, S. Eden, M. Thomson, and H. G. Roskos, Opt. Lett. **29**, 1120 (2004).
3. T. Bartel, P. Gaal, K. Reimann, M. Woerner, and T. Elsaesser, Opt. Lett. **30**, 2805 (2005).
4. X. Xie, J. Dai, and X.-C. Zhang, Phys. Rev. Lett. **96**, 075005 (2006).
5. K. Y. Kim, J. H. Glownia, A. J. Taylor, and G. Rodriguez, Opt. Express **15**, 4577 (2007).
6. K. Y. Kim, A. J. Taylor, J. H. Glownia, and G. Rodriguez, Nat. Photonics **2**, 605 (2008).
7. K. Y. Kim, Phys. Plasmas **16**, 056706 (2009).
8. Y. S. You, T. I. Oh, and K. Y. Kim, Phys. Rev. Lett. **109**, 183902 (2012).
9. T. I. Oh, Y. S. You, N. Jhajj, E. W. Rosenthal, H. M. Milchberg, and K. Y. Kim, Appl. Phys. Lett. **102**, 201113 (2013).
10. L. A. Johnson, J. P. Palastro, T. M. Antonsen, and K. Y. Kim, Phys. Rev. A **88**, 063804 (2013).
11. M. Clerici, M. Peccianti, B. E. Schmidt, L. Caspani, M. Shalaby, M. Giguère, A. Lotti, A. Couairon, F. Légaré, T. Ozaki, D. Faccio, and R. Morandotti, Phys. Rev. Lett. **110**, 253901 (2013).
12. T. I. Oh, Y. J. Yoo, Y. S. You, and K. Y. Kim, Appl. Phys. Lett. **105**, 041103 (2014).
13. I. Babushkin, W. Kuehn, C. Koehler, S. Skupin, L. Berge, K. Reimann, M. Woerner, J. Herrmann, and T. Elsaesser, Phys. Rev. Lett. **105**, 053903 (2010).
14. H. Wen and A. M. Lindenberg, Phys. Rev. Lett. **103**, 023902 (2009).
15. D. Zhang, Z. Lü, C. Meng, X. Du, Z. Zhou, Z. Zhao, and J. Yuan, Phys. Rev. Lett. **109**, 243002 (2012).
16. A. Nguyen, P. González de Alaiza Martínez, J. Déchard, I. Thiele, I. Babushkin, S. Skupin, and L. Bergé, Opt. Express **25**, 4720 (2017).
17. A. Nguyen, P. González de Alaiza Martínez, I. Thiele, S. Skupin, and L. Bergé, Phys. Rev. A **97**, 063839 (2018).
18. A. Nguyen, K. J. Kaltenecker, J.-C. Delagnes, B. Zhou, E. Cormier, N. Fedorov, R. Bouillaud, D. Descamps, I. Thiele, S. Skupin, P. U. Jepsen, and L. Bergé, Opt. Lett. **44**, 1488 (2019).
19. F. Brunel, J. Opt. Soc. Am. B **7**, 521 (1990).
20. N. H. Burnett, C. Kan, and P. B. Corkum, Phys. Rev. A **51**, R3418 (1995).
21. P. B. Corkum, Phys. Rev. Lett. **71**, 1994 (1993).
22. S. Zahedpour, J. K. Wahlstrand, and H. M. Milchberg, Opt. Lett. **40**, 5794 (2015).
23. E. E. Serebryannikov and A. M. Zheltikov, Phys. Rev. Lett. **113**, 043901 (2014).
24. A. M. Zheltikov, J. Phys. B **50**, 092001 (2017).
25. J. Tate, T. Auguste, H. G. Muller, P. Salières, P. Agostini, and L. F. DiMauro, Phys. Rev. Lett. **98**, 013901 (2007).
26. A. D. Shiner, C. Trallero-Herrero, N. Kajumba, H.-C. Bandulet, D. Comtois, F. Légaré, M. Giguère, J.-C. Kieffer, P. B. Corkum, and D. M. Villeneuve, Phys. Rev. Lett. **103**, 073902 (2009).
27. Z. Lü, D. Zhang, C. Meng, X. Du, Z. Zhou, Y. Huang, Z. Zhao, and J. Yuan, J. Phys. B **46**, 155602 (2013).
28. A. Gragossian, D. V. Seletskiy, and M. Sheik-Bahae, Sci. Rep. **6**, 34973 (2016).
29. A. V. Mitrofanov, A. A. Voronin, D. A. Sidorov-Biryukov, A. Pugžlys, E. A. Stepanov, G. Andriukaitis, T. Flöry, S. Ališauskas, A. B. Fedotov, A. Baltuška, and A. M. Zheltikov, Sci. Rep. **5**, 8368 (2015).
30. T. Popmintchev, M.-C. Chen, D. Popmintchev, P. Arpin, S. Brown, S. Ališauskas, G. Andriukaitis, T. Balčiunas, O. D. Mücke, A. Pugzlys, A. Baltuška, B. Shim, S. E. Schrauth, A. Gaeta, C. Hernández-García, L. Plaja, A. Becker, A. Jaron-Becker, M. M. Murnane, and H. C. Kapteyn, Science **336**, 1287 (2012).
31. D. Woodbury, L. Feder, V. Shumakova, C. Gollner, R. Schwartz, B. Miao, F. Salehi, A. Korolov, A. Pugžlys, A. Baltuška, and H. M. Milchberg, Opt. Lett. **43**, 1131 (2018).
32. V. G. Dmitriev, G. G. Gurzadyan, and D. N. Nikogosyan, *Handbook of Nonlinear Optical Crystals* (Springer, 1999).
33. K. Kato, F. Tanno, and N. Umemura, Appl. Opt. **52**, 2325 (2013).
34. X. Zhou, J. X. Cheng, Y. B. Zhou, T. Cao, H. Hong, Z. M. Liao, S. W. Wu, H. L. Peng, K. H. Liu, and D. P. Yu, J. Am. Chem. Soc. **137**, 7994 (2015).
35. M. Kolesik and J. V. Moloney, Phys. Rev. E **70**, 036604 (2004).
36. S. Zahedpour, S. W. Hancock, and H. M. Milchberg, Opt. Lett. **44**, 843 (2019).
37. U. Sapaev, A. Husakou, and J. Herrmann, Opt. Express **21**, 25582 (2013).
38. T. Balciunas, A. J. Verhoef, A. V. Mitrofanov, G. Fan, E. E. Serebryannikov, M. Y. Ivanov, A. M. Zheltikov, and A. Baltuska, Chem. Phys. **414**, 92 (2013).